

Strain-tuned electronic and valley-related properties in Janus monolayers of $SWSiX_2$(X = N, P, As)

Yunxi Qi(戚云西), Jun Zhao(赵俊), and Hui Zeng(曾晖)

Citation: Chin. Phys. B, 2024, 33 (**9**): 096302. DOI: 10.1088/1674-1056/ad6077
Journal homepage: http://cpb.iphy.ac.cn; http://iopscience.iop.org/cpb

What follows is a list of articles you may be interested in

Synthesis and thermoelectric properties of Bi-doped SnSe thin films

Jun Pang(庞军), Xi Zhang(张析), Limeng Shen(申笠蒙), Jiayin Xu(徐家胤), Ya Nie(聂娅), and Gang Xiang(向钢)
Chin. Phys. B, 2021, 30 (**11**): 116302. DOI: 10.1088/1674-1056/ac11da

Inverted V-shaped evolution of superconducting temperature in SrBC under pressure

Ru-Yi Zhao(赵如意), Xun-Wang Yan(闫循旺), and Miao Gao(高淼)
Chin. Phys. B, 2021, 30 (**7**): 076301. DOI: 10.1088/1674-1056/abfbcc

Two-dimensional MnN utilized as high-capacity anode for Li-ion batteries

Junping Hu(胡军平), Zhangyin Wang(王章寅), Genrui Zhang(张根瑞), Yu Liu(刘宇), Ning Liu(刘宁), Wei Li(李未), Jianwen Li(李健文), Chuying Ouyang(欧阳楚英), and Shengyuan A. Yang(杨声远)
Chin. Phys. B, 2021, 30 (**4**): 046302. DOI: 10.1088/1674-1056/abdda8

Effect of strain on electrochemical performance of Janus MoSSe monolayer anode material for Li-ion batteries: First-principles study

Guoqing Wang(王国庆), Wenjing Qin(秦文静), and Jing Shi(石晶)
Chin. Phys. B, 2021, 30 (**4**): 046301. DOI: 10.1088/1674-1056/abca24

Theoretical analysis of cross-plane lattice thermal conduction in graphite

Yun-Feng Gu(顾云风)
Chin. Phys. B, 2019, 28 (**6**): 066301. DOI: 10.1088/1674-1056/28/6/066301

Strain-tuned electronic and valley-related properties in Janus monolayers of SWSiX_2 (X = N, P, As)

Yunxi Qi(戚云西)[1], Jun Zhao(赵俊)[1,†], and Hui Zeng(曾晖)[2,‡]

[1] *New Energy Technology Engineering Laboratory of Jiangsu Province & School of Science, Nanjing University of Posts and Telecommunications, Nanjing* 210023, *China*

[2] *School of Microelectronics, Nanjing University of Science and Technology, Nanjing* 210094, *China*

(Received 7 March 2024; revised manuscript received 27 May 2024; accepted manuscript online 9 July 2024)

Exploring novel two-dimensional (2D) valleytronic materials has an essential impact on the design of spintronic and valleytronic devices. Our first principles calculation results reveal that the Janus SWSiX_2 (X = N, P, As) monolayer has excellent dynamical and thermal stability. Owing to strong spin–orbit coupling (SOC), the SWSiX_2 monolayer exhibits a valence band spin splitting of up to 0.49 eV, making it promising 2D semiconductor for valleytronic applications. The opposite Berry curvatures and optical selection rules lead to the coexistence of valley and spin Hall effects in the SWSiX_2 monolayer. Moreover, the optical transition energies can be remarkably modulated by the in-plane strains. Large tensile (compressive) in-plane strains can achieve spin flipping in the $SWSiN_2$ monolayer, and induce both $SWSiP_2$ and $SWSiAs_2$ monolayers transit from semiconductor to metal. Our research provides new 2D semiconductor candidates for designing high-performance valleytronic devices.

Keywords: first-principles calculations, two-dimensional, valleytronic, spintronic

PACS: 63.20.dk, 68.35.–p, 72.25.Dc, 73.63.–b **DOI:** 10.1088/1674-1056/ad6077

1. Introduction

The degree of freedom and related contrasting transmission properties of the valley provide a new direction for the fabrication of high-performance spintronic devices.[1,2] As a local extremum within the band, the non-equilibrium distribution of charge carriers within valleys that degenerate but not equivalent can be used to achieve information encoding.[3–5] Furthermore, the distance between different valleys in momentum space is relatively large, leading to suppression of intervalley scattering.[6,7] Pioneering research on valleytronics initially relied on traditional semiconductors such as aluminum arsenide quantum wells and silicon.[8,9] However, the manipulation of valley indices is hindered by distinguishing different valleys in these systems.

In recent years, the successful synthesis of two-dimensional (2D) graphene has sparked extensive interest in valleytronics.[10] Research indicates that 2D transition-metal dichalcogenides (TMDs), such as the MoS_2 and WSe_2 monolayers, are suitable materials for manipulating spin and valley.[11,12] The inversion symmetry breaking and strong spin–orbit coupling (SOC) result in opposite transport coefficients and optical selection at the two valleys. Some emergent phenomena, such as valley Hall effect, spin Hall effect, and valley-resolved optical selection rules, can be obtained in 2D monolayer.[3,4,13,14] However, the small growth size and low carrier mobility impede the application of 2D MoS_2 for valleytronics.[15,16] Searching for high-performance materials is crucial for the development of valleytronics. Recently, the MA_2Z_4 family with a seven-layer atomic structure (Z–A–Z–M–Z–A–Z) has been experimentally synthesized by chemical vapor deposition.[17] Compared to the MoS_2 monolayer, the MA_2Z_4 family exhibits a larger size, higher photo-generated carrier mobility, indicating its potential advantages for valleytronic devices.[17–22] Moreover, previous studies have shown that some outstanding electronic, optoelectronic, and catalytic properties can be obtained by constructing various MA_2Z_4-based van der Waals (vdW) heterostructures.[23–28]

Recently, a new class of Janus $XMAZ_2$ (X = S, Se, Te; M = Mo, W, V, Cr; A = Si, Ge; Z = N, P, As) monolayers has been proposed.[29–38] These materials are considered as modifications of the MA_2Z_4 monolayer. Previous investigations have shown that nontrivial topological phase can be induced by using a small strain in the VSi_2N_4 monolayer, Janus $SVSiN_2$ monolayer, and $SVGeN_2$ monolayer, facilitating the achievement of dissipationless transport for device application.[39–42] Furthermore, the Janus nanostructure could give rise to exotic electronic properties such as Rashba spin splitting.[32] In this Letter, we propose a 2D Janus SWSiX_2 (X = N, P, As) derived from the WSi_2N_4 monolayer, where S atoms substitute the N atoms on one side of the WN_2 and the Si–N layer on the same side is removed. Based on density functional theory (DFT) calculation, we establish that the SWSiX_2 monolayer is a candidate for valleytronics. The SWSiX_2 monolayer exhibits dynamical and thermal stabil-

†Corresponding author. E-mail: zhaojun@njupt.edu.cn
‡Corresponding author. E-mail: zenghui@njust.edu.cn

© 2024 Chinese Physical Society and IOP Publishing Ltd

ity, which is consistent with previous studies.[30,31] Significant spin splitting at valence bands of the SWSiX_2 monolayer is achieved due to strong SOC. The SWSiX_2 monolayer exhibits a co-existence of anomalous valley Hall effect and spin Hall effect. Moreover, in-plane strains can effectively tune the spin splitting and optical transition energy at the valley for the SWSiX_2 monolayers. Specifically, an in-plane strain of -2% to 6% can reduce the conduction band splitting of $SWSiN_2$ monolayer at the $K/-K$ valley. It is predicted that 6% strain-driven spin flipping at the $K/-K$ valley can be obtained at the bottom of conduction band for the $SWSiN_2$ monolayer. Both $SWSiP_2$ and $SWSiAs_2$ monolayers experience a transition from semiconductor to metal. Our findings offer promising candidates for the design of spintronic devices.

2. Computational methods

We use Vienna *ab initio* simulation package (VASP) to study the electronic structures of the SWSiX_2 monolayers.[43,44] The projected augmented wave (PAW) method is used to describe the interaction between electrons and ions.[45] The Perdew–Burke–Ernzerhof (PBE) methods are used as exchange and correlation functions.[46] The Heyd–Sculeria–Ernzerhof (HSE06) hybrid functional is used to calculate electronic structures for comparison.[47] A vacuum layer of 20 Å is used, and he cutoff energy is set to 500 eV. The convergence criteria for energy and atomic force are set at 1×10^{-8} eV and 1×10^{-4} eV/Å, respectively. The Brillouin zone is sampled by $16\times16\times1$ k-mesh for structural optimization and electronic structure calculations.[48] Based on the density functional perturbation theory (DFPT) method, the phonon dispersion of a $5\times5\times1$ supercell is calculated by PHONOPY code to examine the dynamical stability.[49] The *ab initio* molecular dynamics (AIMD) simulation is performed at 300 K by using a $4\times4\times1$ supercells to determine the thermal stability.[50] The VASPBERRY subroutine is used to calculate the Berry curvature and circular polarization of the SWSiX_2 monolayer.[51] The VASPKIT post-processing tool is used to process calculation results.[52] All atomic structures are visualized by VESTA software.[53]

3. Results and discussion

3.1. Atomic structures

The optimized atomic structure of the SWSiX_2 (X = N, P, As) monolayers is shown in Fig. 1. The SWSiX_2 monolayer has a hexagonal lattice. From the side view, its atomic order is S–W–X–Si–X, consisting of five atomic layers. Compared with the WSi_2N_4 structure, the S atom replaces the N atom on the same side of WN_2 and removes the Si–N layer on the same side. The symmetry of the SWSiX_2 (space group: $P3m1$) is lower than that of the MA_2Z_4 monolayer (space group: $P\bar{6}m2$). Therefore, the SWSiX_2 monolayer can be regarded as a 2D Janus structure with broken inversion symmetry. According to Table 1, the lattice constants of the $SWSiN_2$, $SWSiP_2$, and $SWSiAs_2$ monolayers are increased since the atomic numbers are increased.[54,55]

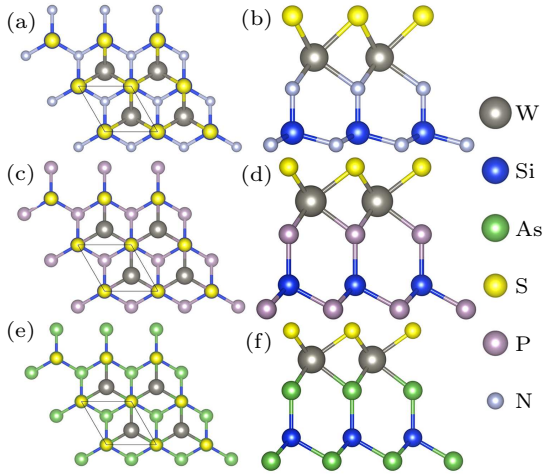


Fig. 1. Top and side views of the Janus $SWSiN_2$ (a)–(b), $SWSiP_2$ (c)–(d), and $SWSiAs_2$ (e)–(f) monolayers. Gray, blue, green, yellow, light purple, and silver white represent W, Si, As, S, P, N atoms, respectively.

Table 1. Lattice constants a and b, elastic constant (C_{11} and C_{12}), bandgap without SOC (E_g), bandgap with SOC (E_g^{SOC}), the spin splitting in the valence band (ΔV), and cohesive energy (E_{coh}).

Structure	$a=b$ (Å)	C_{11} (N/m)	C_{12} (N/m)	E_g (eV)	E_g^{SOC} (eV)	ΔV (eV)	E_{coh} (eV)
$SWSiN_2$	2.989	143.792	32.540	2.31	2.00	0.38	–4.985
$SWSiP_2$	3.381	91.705	21.352	0.97	0.76	0.45	–3.692
$SWSiAs_2$	3.501	84.040	22.143	0.44	0.37	0.49	–3.405

3.2. Structural stabilities and mechanical properties

We explore the stability of SWSiX_2 monolayer via AIMD simulation, phonon spectra, cohesive energy E_{coh}, and Born–Huang mechanical criterion.[56] In Figs. S1(a)–S1(c) of the supporting information, we investigate the thermal stability of the SWSiX_2 monolayer at 300 K via AIMD simulation. The total energies of the three monolayers fluctuate near the equilibrium position, and their atomic structures almost unchanged throughout the entire simulation process. The phonon dispersions are shown in Figs. S1(d)–S1(f). The absence of negative branch verifies the dynamical stability of the SWSiX_2 monolayer. Furthermore, the the cohesive energy E_{coh} is calculated by the following expression:

$$E_{coh} = \frac{[E(\mathrm{SWSi}X_2) - E(\mathrm{S}) - E(\mathrm{W}) - E(\mathrm{Si}) - 2E(X)]}{5}, \quad (1)$$

where $E(\mathrm{SWSi}X_2)$ is the total energy of single-layer $\mathrm{SWSi}X_2$, and E(S), E(W), E(Si), and E(N) are the energies of separated S, W, Si, and N atoms, respectively. The lower the E_{coh} value, the higher the stability. The calculated cohesive energies of the $SWSiN_2$, $SWSiP_2$, and $SWSiP_2$ monolayers are -4.985 eV/atom -3.692 eV/atom, and -3.405 eV/atom, respectively. It indicates that these $\mathrm{SWSi}X_2$ monolayers are energetically favorable to be synthesized in experiments.

Furthermore, we also analyze the elastic constant (C_{ij}) of the 2D Janus $SWSiN_2$ ($SWSiP_2$ and $SWSiAs_2$) monolayer. Two independent parameters C_{11} and C_{12} are obtained, which are listed in Table 1. The calculation results indicate that the $\mathrm{SWSi}X_2$ monolayers satisfy Born–Huang stability criterion: $C_{11} > 0$ and $C_{11}^2 > C_{12}^2$. This confirms the mechanical stability of the $\mathrm{SWSi}X_2$ monolayer. Considering that strain is a key mechanism for regulating the monolayer valleytronic properties, we plotted the Young's modulus of $SWSiN_2$ ($SWSiP_2$ and $SWSiAs_2$) monolayer, as shown in Fig. S2 of the supporting information. The Young's modulus is 136.387 N/m (86.446 N/m and 78.188 N/m). $\mathrm{SWSi}X_2$ monolayer exhibits excellent flexible mechanical properties.

3.3. Electronic structures

The electronic properties of the $SWSiN_2$ monolayer are shown in Fig. 2. Additionally, figures S3 and S4 correspond to the $SWSiP_2$ and the $SWSiAs_2$ monolayers, respectively. Figures 2(a) and 2(b) show the band structure of the $SWSiN_2$ monolayer without SOC under different functionals (PBE and HSE06). The $SWSiN_2$ monolayer is a semiconductor with an indirect bandgap of 2.31 eV (HSE06 bandgap of 2.84 eV). The valence band maximum (VBM) is located at the $K/-K$ valley, forming a pair of degenerate valleys. The highest unoccupied state of the $SWSiN_2$ monolayer forms a local energy minimum at the $K/-K$ valleys. The band structures of the $SWSiP_2$ and the $SWSiAs_2$ monolayers are similar to that of the $SWSiN_2$ monolayers, as shown in Figs. S3(a), S3(b) and S4(a), S4(b) of the supporting information. Compared with the $SWSiN_2$ monolayer, the bandgaps of the $SWSiP_2$ and $SWSiAs_2$ monolayers are reduced to 0.97 eV and 0.44 eV, respectively, which are larger than the bandgaps of the WSi_2X_4 (X = N, P, As).[54,55,57] The above results are consistent with previous studies.[30,33] When the SOC is not taken into account, the VBM of the of the $SWSiP_2$ and $SWSiAs_2$ monolayers is located at the G-point, and their conduction band minimum (CBM) are located at the $K/-K$ valleys. Figures 2(a), 2(b), S3(a), S3(b), and S4(a), S4(b) of the supporting information clearly show that the characteristics of the electronic band obtained by GGA and HSE06 are consistent with each other, i.e., $SWSiN_2$, $SWSiAs_2$, and $SWSiP_2$ monolayers exhibit indirect bandgaps when spin–orbit coupling is not considered. Therefore, we study the electronic properties of the monolayered $\mathrm{SWSi}X_2$ by using the PBE functional hereafter. For the $\mathrm{SWSi}X_2$ monolayer, its local energy minima are located at the $K/-K$ valleys, facilitating its practical application for 2D valleytronics.

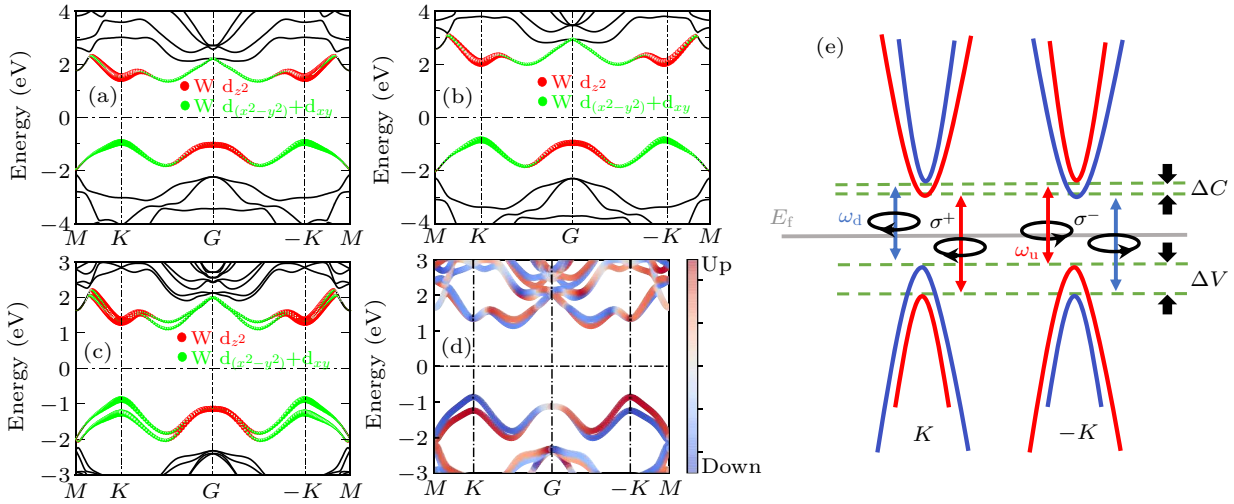


Fig. 2. The projected band structures of the Janus $SWSiN_2$ monolayer obtained from (a) PBE functional and (b) HSE06 functional, respectively. The (c) projected band structure obtained from PBE+SOC, and (d) the corresponding band structure with opposite spin components along z direction (red is up; blue is down). The Fermi level is set to 0 eV. (e) Schematic diagram of valley spin splitting at the $K/-K$ valley. The red and blue parabolas represent spin-up and spin-down, respectively. The red and blue arrows represent the optical transition energy at ω_u and ω_d frequencies.

The VBM and CBM of the $\mathrm{SWSi}X_2$ monolayer are mainly contributed by the d-orbitals of W atoms, and the p orbitals of X and S atoms also have small contributions, as shown in Fig. S5. We calculate the band structures with SOC. Owing to the strong SOC of W atoms, all the $\mathrm{SWSi}X_2$ monolayers exhibit significant band splitting. For the the $SWSiN_2$ and the $SWSiAs_2$ monolayers shown in Figs. 2(c) and S4(c), the band characteristics remain unchanged when considering SOC, and the bandgaps decreases to 2.00 eV and 0.37 eV, respectively. For the $SWSiP_2$ monolayer in Fig. S3(c), considering that the top valence band of the $K/-K$ valleys with SOC is higher than the valence band of the G-point, based on the intrinsic

properties of SOC, the $SWSiP_2$ monolayer is a semiconductor with a direct bandgap of 0.76 eV. Rudi *et al.* found that the bandgaps of $SWSiN_2$ monolayer and $SWSiP_2$ monolayer under PBE + SOC were 2.06 eV and 0.74 eV, respectively, which are similar to our results.[30] For the $SWSiX_2$ semiconductor, the valley characteristics and orbital contributions in the valence and conduction bands remain unchanged under SOC.

The inclusion of SOC leads to significant spin splitting at the $K/-K$ valley of the $SWSiX_2$ monolayer, as shown in Figs. 2(d), S3(d), and S4(d). Similar to the $W/MoSi_2X_4$ (X = N, P, As) monolayer,[54,55,57,58] the intensity of spin splitting in the $SWSiX_2$ system increases with the increment of atomic number of X atoms. In Fig. 2(e), we show the enlarged details of the $K/-K$ valley. Specifically, the spin splitting in the valence bands (ΔV) of $SWSiN_2$, $SWSiP_2$, and $SWSiAs_2$ monolayers are 0.38 eV, 0.45 eV, and 0.49 eV, respectively, which is much higher than that of the MoS_2 monolayer.[57] Our calculated results agree well with previous investigation regarding to the valence band spin splitting of the $SWSiN_2$ monolayer ($\Delta V = 0.382$ eV) and $SWSiP_2$ monolayer ($\Delta V = 0.462$ eV),[30] ensuring the reliability of our theoretical study. Compared with the ΔV, the spin splitting of the conduction bands (ΔC) is much smaller. In addition, in Figs. 2(e), S3(e), and S4(e), the highest occupied state at the K ($-K$) valley of the $SWSiX_2$ monolayer is contributed by spin-down (spin-up) state. For the conduction band, the lowest unoccupied state at the K ($-K$) valley of the $SWSiN_2$ monolayer is governed by spin-up (spin-down) state, which is opposite to $SWSiP_2$ and $SWSiAs_2$ monolayers. Owing to the spin splitting, the optical transition energy ω_u (ω_d) of $SWSiN_2$, $SWSiP_2$, and $SWSiAs_2$ monolayers is 2.58 (2.22) eV, 1.22 (0.76) eV and, 1.10 (0.57) eV, respectively. In addition, we constructed Wannier functionals and obtained the corresponding tight-binding (TB) Hamiltonians using the maximum localized Wannier function (MLWFs).[59] The VBM and CBM of the $SWSiX_2$ monolayer are mainly dominated by d_{z^2}, d_{xy}, and $d_{x^2-y^2}$ orbitals of the W atoms. In order to reproduce the effective model of low-energy states by using MLWFs, we consider the d orbitals of W atoms, p orbitals of S atoms, and p orbitals of X atoms as initial Wannier basis to establish our TB model, as shown in Fig. S6. The electronic bands fitted by the TB model are well consistent with our first principles calculation results, ensuring that the TB Hamiltonians could accurately describe the valley-related properties of the $SWSiX_2$ monolayer. In summary, compared to the $SWSiN_2$ monolayer, the larger spin splitting and relatively moderate optical transition energy in the $SWSiP_2$ and $SWSiAs_2$ monolayers are beneficial for establishing robust valley–spin coupling.

3.4. Valley-related properties

The spin splitting at the $K/-K$ valley of the $SWSiN_2$ monolayer is significantly correlated with SOC intensity. To explain the difference in spin splitting between the valence and conduction bands of the $SWSiX_2$ monolayer, we calculate the SOC intensity of the W-d orbitals in the $SWSiX_2$ monolayer, as shown in Fig. S7. It can be seen that the SOC intensity in the $SWSiX_2$ monolayer is mainly dominated by the $d_{xy}/d_{x^2-y^2}$ orbitals, while the valence band at the $K/-K$ valley are mainly contributed by the $d_{xy}/d_{x^2-y^2}$ orbitals. The large spin splitting of the $SWSiX_2$ monolayer in the valence band is closely related to the $d_{xy}/d_{x^2-y^2}$ orbitals. The conduction band at the $K/-K$ valley of the $SWSiX_2$ monolayer is mainly contributed by d_{z^2} orbitals, and the $d_{xy}/d_{x^2-y^2}$ orbitals have observable contributions. Figure S7 shows that the SOC intensity of $d_{z^2}/d_{x^2-y^2}$ orbitals and d_{z^2}/d_{xy} in the $SWSiX_2$ monolayer is almost zero, leading to almost zero spin splitting in the conduction band of the $SWSiX_2$ monolayer.

Different valley spin splitting can lead to spin or valley Hall effect. To confirm the non-equivalent valences at K and $-K$ in the $SWSiX_2$ monolayer, we investigate the nonzero out of plane Berry curvature $\Omega_z(k)$:

$$\Omega_z(k) = -\sum_n \sum_{n\neq n'} f_n \frac{2\,\mathrm{Im}\left\langle \psi_{nk}\left|v_x\right|\psi_{n'k}\right\rangle \left\langle \psi_{n'k}\left|v_y\right|\psi_{nk}\right\rangle}{\left(E_n - E_n'\right)^2}, \quad (2)$$

where f_n is the equilibrium Fermi–Dirac distribution function, ψ_{nk} and E_n is the Bloch wave function and its eigenvalues, υ_x, υ_y is the velocity operator along different components.[55,60] Owing to the inversion symmetry breaking and time reversal symmetry breaking in the $SWSiX_2$ monolayer, it is anticipated that the Berry curvatures at the K and $-K$ valleys should be opposite, i.e., $\Omega_z(-k) = -\Omega_z(k)$. Figures 3(a) and S8 confirm our prediction. The Berry curvatures of the $SWSiX_2$ monolayer near the $K/-K$ valleys possess the same values but opposite signs. In addition, the Berry curvature of the $SWSiX_2$ monolayer at the $K/-K$ valley increases with the increase of X atomic number. Combined with an in-plane electric field, it is expected that carriers near the $K/-K$ valley will acquire different anomalous lateral velocities, as shown in Fig. 3(c). When the injected carriers are between the two spin states of the valence band at the valley, the carriers with opposite spin states will accumulate on opposite boundaries due to the opposite Berry curvatures at the K and $-K$ valleys. Consequently, the valley and spin Hall effect can be obtained in the $SWSiX_2$ monolayer.

The non-equivalent $K/-K$ valleys and Berry curvature indicate that $K/-K$ valley has chirality, which can be described by circularly polarized light selection rules. Circular polarization is defined as

$$\eta(\boldsymbol{k}) = \frac{|P_+(\boldsymbol{k})|^2 - |P_-(\boldsymbol{k})|^2}{|P_+(\boldsymbol{k})|^2 + |P_-(\boldsymbol{k})|^2}, \quad (3)$$

where $P_\pm(\boldsymbol{k}) = \left\langle c\boldsymbol{k}\left|p_x \pm \mathrm{i}\,p_y\right|v\boldsymbol{k}\right\rangle$ are the inter-band transition matrices, which describe vertical transition from valence band (υ) to conduction band (c) in the $\boldsymbol{k}$-space stimulated by left-

and right-handed circularly polarized light, respectively.[61] As shown in Figs. 3(b) and S8, left-handed (right-handed) circularly polarized light can be selectively absorbed at the $-K$ (K) valley, while right-handed (left-handed) light is completely suppressed. Therefore, circularly polarized light pumping can selectively generate electrons and holes in a desired valley in the SWSiX_2 monolayer, as shown in Fig. 3(d). Optically generated carriers selectively excited by circularly polarized light will obtain opposite transverse velocities due to their opposite Berry curvatures. This is similar to the situation in 2D MoS_2.[6] In addition, the $SWSiP_2$ monolayer has a direct bandgap located at the $K/-K$ valleys, facilitating the manipulation of valley-related properties by optical and electrical excitation.[62] Correspondingly, the $SWSiP_2$ monolayer is a promising candidate for valleytronic application. The $SWSiP_2$ monolayer exhibits approximately 100% valley-contrasting physics.

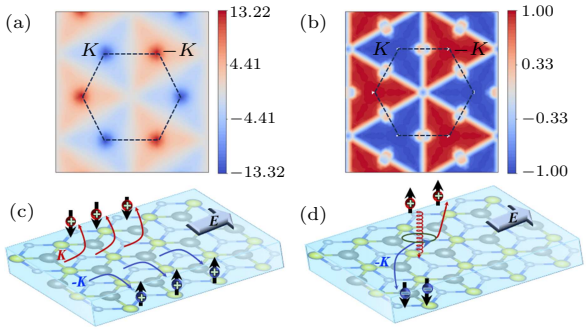


Fig. 3. (a) Berry curvature and (b) circularly polarized polarization of the Janus monolayer $SWSiN_2$. (c) Schematic diagrams of valley and spin Hall effects under hole doping and (d) right-handed polarized light irradiation in the SWSiX_2 monolayer. The up/down arrows indicate spin up/spin down. The ± symbol in the ball represents holes/electrons.

3.5. Strain engineering

Strain engineering is shown to modulate the valley-related properties of 2D monolayers.[63] The magnitude of the in-plane biaxial strain ε is defined as: $\varepsilon = \left(\frac{a-a_0}{a_0}\right) \times 100\%$, where a_0 and a represents the lattice constants without- and with-biaxial strains, respectively. As shown in Figs. 4(a)–4(c), as the strain changes from −6% to 6%, the ΔV of the SWSiX_2 monolayer gradually increases, and the growth rate of ΔV gradually decreases. The variation trend of ΔV in the $SWSiN_2$ monolayer and $SWSiP_2$ monolayer mentioned above are consistent with previous studies.[30,31] For ΔC, as shown in Figs. S9–S11, the spin splitting of the conduction bands for the SWSiX_2 monolayer gradually disappears under −6% and −4% strain modulation. Therefore, when the strain changes from −2% to 6%, the ΔC of the $SWSiP_2$ monolayer gradually increases from 1.51 meV to 7.55 meV. However, the ΔC of the $SWSiN_2$ and the $SWSiAs_2$ monolayers gradually decreases, which is expected to achieve spin flipping in the conduction band at the K valley. As shown in the inset of Fig. 4(a), the lowest unoccupied state of the conduction band at the K valley changes from spin-up to spin-down when the strain changes from 4% to 6%, and the spin flipping is simultaneously obtained at the $-K$ valley. Therefore, the opposite spins at the $K/-K$ valleys are still coupled by time reversal symmetry. Since the ΔC of the $SWSiAs_2$ monolayer gradually decreases with the increase of strain, spin flipping phenomenon does not occur.

For the optical transition energy ω_u/ω_d of the SWSiX_2 monolayer, as shown in Figs. 4(d)–4(f), it is found that the ω_u/ω_d is monotonously decreased when the strain is changed from −2% to 6%. Figure S8 indicates that the $SWSiP_2$ can achieve semiconductor–metal transition under large in-plane tensile. Similar semiconductor–metal transition is also observed for the $SWSiAs_2$ monolayer when $\varepsilon \geq 4\%$ and $\varepsilon \leq -6\%$. Compared to the modulation of the spin splitting, the strain engineering has more significant influence on the optical transition.

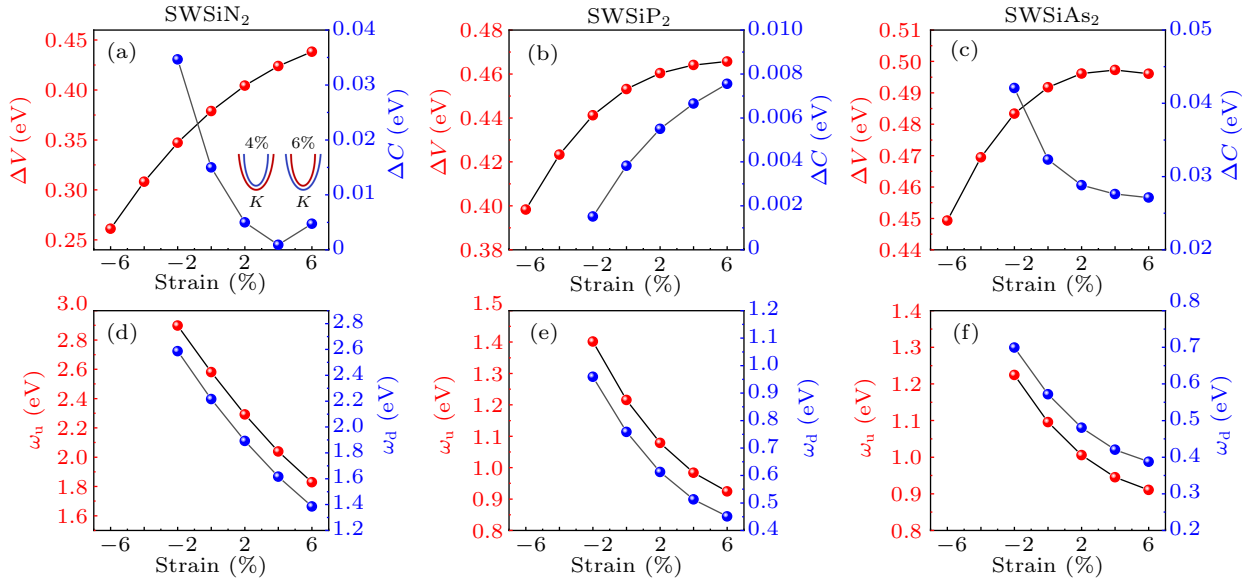


Fig. 4. (a)–(c) spin splittings and (d)–(f) optical transition energies under different in-plane strains. Panels (a) and (d) are the calculated results for the $SWSiN_2$ monolayer; panel (b) and (e) are corresponding results for $SWSiP_2$ monolayer; panels (c) and (f) are the corresponding results for the $SWSiAs_2$ monolayer. The inset in panel (a) illustrates the spin flipping at the K valley when the strains change from 4% to 6%.

4. Conclusions

In summary, our calculations show that the 2D Janus SWSiX_2 monolayer with inversion symmetry breaking and strong SOC arising from W-d_{xy}/$d_{x^2-y^2}$ orbitals gives rise to significant spin splitting in the valence band. In particular, the $SWSiP_2$ monolayer has a direct band gap located at the $K/-K$ valley, making it most promising candidate to achieve valleytronics. The opposite Berry curvatures and the optical selection rule result in the coexistence of valley and spin Hall effects in the SWSiX_2 monolayer. The in-plane strain could sensitively modulate the optical transition energy. Large in-plane tensile (compressive) strain can induce semiconductor-to-metal transition for the $SWSiP_2$ and $SWSiAs_2$ monolayers, and the spin flipping can be achieved for the $SWSiN_2$ monolayer.

Acknowledgements

Project supported by the National Natural Science Foundation of China (Grant Nos. 62174088 and 62371238). We are grateful to the High-Performance Computing Centre of Nanjing University for providing the IBM Blade cluster system.

References

[1] Schaibley J R, Yu H, Clark G, Rivera P, Ross J S, Seyler K L, Yao W and Xu X 2016 *Nat. Rev. Mater.* **1** 16055
[2] He M, Rivera P, Tuan D V, Wilson N P, Yang M, Taniguchi T, Watanabe K, Yan J, Mandrus D G, Yu H, Dery H, Yao W and Xu X 2020 *Nat. Commun.* **11** 618
[3] Xiao D, Yao W and Niu Q 2007 *Phys. Rev. Lett.* **99** 236809
[4] Zeng H, Dai J, Yao W, Xiao D and Cui X 2012 *Nat. Nanotechnol.* **7** 490
[5] Kim Y and Lee J D 2019 *Phys. Rev. Appl.* **11** 034048
[6] Xiao D, Liu G B, Feng W, Xu X and Yao W 2012 *Phys. Rev. Lett.* **108** 196802
[7] Xu L, Yang M, Shen L, Zhou J, Zhu T and Feng Y P 2018 *Phys. Rev. B* **97** 041405
[8] Ohkawa F J and Uemura Y 1977 *J. Phys. Soc. Jpn.* **43** 917
[9] Gunawan O, Habib B, De Poortere E P and Shayegan M 2006 *Phys. Rev. B* **74** 155436
[10] Novoselov K S, Geim A K, Morozov S V, Jiang D, Zhang Y, Dubonos S V, Grigorieva I V and Firsov A A 2004 *Science* **306** 666
[11] Mak K F, He K, Shan J and Heinz T F 2012 *Nat. Nanotechnol.* **7** 494
[12] Singh N and Schwingenschlogl U 2017 *Adv. Mater.* **29** 1600970
[13] Qian X, Liu J, Fu L and Li J 2014 *Science* **346** 1344
[14] Mak K F, McGill K L, Park J and McEuen P L 2014 *Science* **344** 1489
[15] Chang M C, Ho P H, Tseng M F, Lin F Y, Hou C H, Lin I K, Wang H, Huang P P, Chiang C H, Yang Y C, Wang I T, Du H Y, Wen C Y, Shyue J J, Chen C W, Chen K H, Chiu P W and Chen L C 2020 *Nat. Commun.* **11** 3682
[16] Radisavljevic B, Radenovic A, Brivio J, Giacometti V and Kis A 2011 *Nat. Nanotechnol.* **6** 147
[17] Hong Y L, Liu Z, Wang L, Zhou T, Ma W, Xu C, Feng S, Chen L, Chen M L, Sun D M, Chen X Q, Cheng H M and Ren W 2020 *Science* **369** 670
[18] Zhao H, Yang G, Liu Y, Yang X, Gu Y, Wei C, Xie Z, Zhang Q, Bian B, Zhang X, Huo X and Lu N 2021 *ACS Appl. Electron. Mater.* **3** 5086
[19] Yuan J, Wei Q, Sun M, Yan X, Cai Y, Shen L and Schwingenschlögl U 2022 *Phys. Rev. B* **105** 195151
[20] Hasani N, Shalchian M, Rajabi-Maram A and Touski S B 2023 *IEEE Trans. Electron Dev.* **70** 5415
[21] Nandan K, Bhowmick S, Chauhan Y S and Agarwal A 2023 *Phys. Rev. Appl.* **19** 064058
[22] Sheoran S, Monga S, Phutela A and Bhattacharya S 2023 *J. Phys. Chem. Lett.* **14** 1494
[23] Zhao J, Jin X, Zeng H, Yao C and Yan G 2021 *Appl. Phys. Lett.* **119** 213101
[24] Cao L, Zhou G, Wang Q, Ang L K and Ang Y S 2021 *Appl. Phys. Lett.* **118** 013106
[25] Zhang X, Zheng J Y, Xiang Y C, Wu D, Fan J, Sun Y Y, Chen L J, Gan L Y and Zhou X 2023 *Appl. Phys. Lett.* **123** 023505
[26] Cao L, Deng X, Tang Z k, Tan R and Ang Y S 2024 *J. Mater. Chem. C* **12** 648
[27] Qi Y, Yao C, Zhao J and Zeng H 2023 *Phys. Chem. Chem. Phys.* **25** 28104
[28] Tho C C, Guo S D, Liang S J, Ong W L, Lau C S, Cao L, Wang G and Ang Y S 2023 *Appl. Phys. Rev.* **10** 041307
[29] Guo S D, Mu W Q, Zhu Y T, Han R Y and Ren W C 2021 *J. Mater. Chem. C* **9** 2464
[30] Rudi S G, Soleimani-Amiri S, Rezavand A and Ghobadi N 2023 *J. Phys. Chem. Solids* **181** 111561
[31] Nguyen H T, Cuong N Q, Vi V T T, Hieu N N and Tran L P T 2023 *Phys. Chem. Chem. Phys.* **25** 21468
[32] Zhao J, Qi Y, Yao C and Zeng H 2024 *Phys. Rev. B* **109** 035408
[33] Geng L, Chen K, Lu H, Wang S and Yang Y 2023 *Phys. Chem. Chem. Phys.* **25** 32021
[34] Sibatov R T, Meftakhutdinov R M and Kochaev A I 2022 *Appl. Surf. Sci.* **585** 152465
[35] Nguyen S T, Cuong P V, Cuong N Q and Nguyen C V 2022 *Dalton Trans.* **51** 14338
[36] Gao Z, He Y and Xiong K 2023 *Dalton Trans.* **52** 17416
[37] Tran P T L, Hieu N V, Bui D H, Cuong Q N and Hieu N N 2023 *Nanoscale Adv.* **5** 3104
[38] Dong M M, He H, Niu Y, Wang C K and Fu X X 2023 *ACS Appl. Nano Mater.* **6** 1541
[39] Sun Z, Li X, Zhao Z, Zeng Y, Wei Y and Wang J 2023 *J. Mater. Chem. C* **11** 9815
[40] Zhao J, Qi Y, Yao C and Zeng H 2024 *Appl. Phys. Lett.* **124** 093103
[41] Qi Y, Yao C, Zhao J and Zeng H 2024 *J. Mater. Chem. C* **12** 4417
[42] Chen H X, Yuan X B and Ren J F 2024 *Chin. Phys. B* **33** 047304
[43] Kresse G and Furthmüller J 1996 *Phys. Rev. B* **54** 11169
[44] Kresse G and Hafner J 1993 *Phys. Rev. B* **47** 558
[45] Blöchl P E 1994 *Phys. Rev. B* **50** 17953
[46] Perdew J P, Burke K and Ernzerhof M 1996 *Phys. Rev. Lett.* **77** 3865
[47] Heyd J and Scuseria G E 2004 *J. Chem. Phys.* **121** 1187
[48] Monkhorst H J and Pack J D 1976 *Phys. Rev. B* **13** 5188
[49] Togo A, Oba F and Tanaka I 2008 *Phys. Rev. B* **78** 134106
[50] Barnett R N and Landman U 1993 *Phys. Rev. B* **48** 2081
[51] Kim S W, Kim H J, Cheon S and Kim T H 2022 *Phys. Rev. Lett.* **128** 046401
[52] Wang V, Xu N, Liu J C, Tang G and Geng W T 2021 *Comput. Phys. Commun.* **267** 108033
[53] Momma K and Izumi F 2011 *J. Appl. Crystallogr.* **44** 1272
[54] Qi Y, Yao C, Zhao J and Zeng H 2023 *Phys. Rev. B* **108** 125304
[55] Ke C, Wu Y, Yang W, Wu Z, Zhang C, Li X and Kang J 2019 *Phys. Rev. B* **100** 195435
[56] Andrew R C, Mapasha R E, Ukpong A M and Chetty N 2012 *Phys. Rev. B* **85** 125428
[57] Kormányos A, Zólyomi V, Drummond N D, Rakyta P, Burkard G and Fal'ko V I 2013 *Phys. Rev. B* **88** 045416
[58] Ai H, Liu D, Geng J, Wang S, Lo K H and Pan H 2021 *Phys. Chem. Chem. Phys.* **23** 3144
[59] Mostofi A A, Vanderbilt D, Souza I, Yates J R, Marzari N and Lee Y S 2008 *Comput. Phys. Commun.* **178** 685
[60] Yao Y, Kleinman L, MacDonald A H, Sinova J, Jungwirth T, Wang D S, Wang E and Niu Q 2004 *Phys. Rev. Lett.* **92** 037204
[61] Cao T, Wang G, Han W, Ye H, Zhu C, Shi J, Niu Q, Tan P, Wang E, Liu B and Feng J 2012 *Nat. Commun.* **3** 887
[62] Mak K F, Xiao D and Shan J 2018 *Nat. Photon.* **12** 451
[63] Qi Y, Sadi M A, Hu D, Zheng M, Wu Z, Jiang Y and Chen Y P 2023 *Adv. Mater.* **35** 2205714